Numerical Aspects of 3D Stellar Winds

A. Strugarek[1,2], A. S. Brun[2], S. P. Matt[3], V. Reville[2]

[1]*Département de physique, Université de Montréal, C.P. 6128 Succ. Centre-Ville, Montréal, QC H3C-3J7, Canada*

[2]*Laboratoire AIM Paris-Saclay, CEA/Irfu Université Paris-Diderot CNRS/INSU, F-91191 Gif-sur-Yvette.*

[3]*Astrophysics group, School of Physics, University of Exeter, Stocker Road, Exeter EX4 4QL, UK*

Abstract. This paper explores and compares the pitfalls of modelling the three-dimensional wind of a spherical star with a cartesian grid. Several numerical methods are compared, using either uniform and stretched grid or adaptive mesh refinement (AMR). An additional numerical complication is added, when an orbiting planet is considered. In this case a rotating frame is added to the model such that the orbiting planet is at rest in the frame of work. The three-dimensional simulations are systematically compared to an equivalent two-dimensional, axisymmetric simulation. The comparative study presented here suggests to limit the rotation rate of the rotating frame below the rotating frame of the star and provides guidelines for further three-dimensional modelling of stellar winds in the context of close-in star-planet interactions.

1. Introduction

Magnetized stellar winds have long been recognized as the major source of angular momentum extraction in main sequence stars (Parker 1958; Weber & Davis 1967; Mestel 1968). In order to reliably assess the stellar wind torque, the acceleration profile and the magnetic field geometry of the wind are needed. It was recently demonstrated that, in particular, complex magnetic topologies of cool stars could significantly alter the torque (see, *e.g.* Cohen & Drake 2014; Réville et al. 2014) compared to more simple topologies. Three dimensional numerical simulations provide today a reliable way to compute, in a dynamically self-consistent way, the torque arising from stellar wind with complex magnetic fields for a large variety of stars.

However, no consensual parametrization of fully three-dimensional, non-axisymmetric stellar wind torques has yet been proposed in the literature.

Furthermore, the growing number of know exoplanets triggered renewed interest in the recent years in the interactions existing between star and close-in planets (for a recent review, see Lanza 2014, in this volume). In particular, close-in planets can magnetically interact with their host, which leads to a direct transfer of angular momentum due to a magnetic link between the two objects (among numerous other effects as well, see, *e.g.*, Cuntz et al. 2000; Zarka 2007; Scharf 2010; Vidotto et al. 2014, and references there in). Several analytical studies (*e.g.*, Lanza 2009; Laine & Lin 2011, and references therein) have been pursued in the past years to better constrain our understanding of this angular momentum transfer. In a recent work, Strugarek et al. (2014) explored the efficiency of the angular momentum transfer as a function of the relative position of the orbiting planet in the stellar wind and of the topology of the planetary field with 2.5D simulations. In order to validate the trends they found, 3D numerical simulations taking into account the adequate geometry of the problem are needed (see Cohen et al. 2009, for an example of such global modelling).

We report here an ongoing effort in developing magnetohydrodynamics (MHD) simulations of the stellar winds of cool stars in three dimensions. We consider one-fluid and ideal models of stellar winds which are very simple compared to more recent solar wind models (see, *e.g.*, Oran et al. 2013; Sokolov et al. 2013). However, they inherit important conservation properties from their 2.5D counterparts (see Strugarek et al. 2012, and section 3.2). We show in this work that ensuring such conservation properties is mandatory to derive physically meaningful global trends from grids of numerical simulations. By such, they are thus of particular interest for our understanding of the gyro-chronology of cool stars. In addition, we focus here on the numerical difficulties associated with a rotating frame, anticipating eventual star-planet interactions studies with such stellar wind models.

2.   Modelling stellar winds

Following the preliminary work in 2.5D axisymmetric geometry described in (Strugarek et al. 2014), we adapted our stellar wind model to a 3D cartesian geometry. We implemented the same "3-layer" boundary conditions to improve the conservation properties of our numerical solution. We use the PLUTO code (Mignone et al. 2007) which solves the following set of ideal MHD equations:

$$\partial_t \rho + \boldsymbol{\nabla} \cdot (\rho \mathbf{v}) = 0 \tag{1}$$

$$\partial_t \mathbf{v} + \mathbf{v} \cdot \boldsymbol{\nabla} \mathbf{v} + \frac{1}{\rho} \boldsymbol{\nabla} P + \frac{1}{\rho} \mathbf{B} \times \boldsymbol{\nabla} \times \mathbf{B} = \mathbf{a} \,, \tag{2}$$

$$\partial_t P + \mathbf{v} \cdot \boldsymbol{\nabla} P + \rho c_s^2 \boldsymbol{\nabla} \cdot \mathbf{v} = 0 \,, \tag{3}$$

$$\partial_t \mathbf{B} - \boldsymbol{\nabla} \times (\mathbf{v} \times \mathbf{B}) = 0 \,, \tag{4}$$

where ρ is the plasma density, $\mathbf{v}$ its velocity, P the gas pressure, $\mathbf{B}$ the magnetic field, and $\mathbf{a}$ is composed of gravitational acceleration (which is time-independent) and the Coriolis and centrifugal forces of a rotating frame Ω_0. The sound speed is given by $c_s = \sqrt{\gamma P/\rho}$, with γ the adiabatic exponent. We use an ideal gas equation of state

$$\rho \varepsilon = P / (\gamma - 1) \,, \tag{5}$$

where ε is the specific internal energy. We use an *hll* solver combined with a *minmod* limiter. A second-order Runge-Kutta is used for the time evolution, resulting in an overall second-order accurate numerical method. The solenoidality of the magnetic field is ensured with a constrained transport method in the static grid version of the model, and with Powell's *eight waves* method in the AMR version (see Mignone et al. 2012). We refer the interested reader to (Mignone et al. 2007) for an extensive description of the various methods that PLUTO offers.

The structure of the wind directly depends on three velocity ratios defined at the surface of the star (see, *e.g.*, Matt et al. 2012), and on the ratio of specific heats γ. The three characteristic velocities are the sound speed c_s, the Alfvén speed $v_A = B_\star/\sqrt{4\pi\rho_\star}$ (where $B_\star$ is the magnetic field strength at the stellar equator) and the rotation speed $v_{\rm rot}$ (in this work, the star is considered to rotate as a solid body). Their ratios to the escape velocity $v_{\rm esc} = \sqrt{2GM_\star/R_\star}$ (with $M_\star$ the stellar mass and $R_\star$ the stellar radius) at the stellar surface then define a unique stellar wind solution. We choose for this study the same parameters as in Strugarek et al. (2014), which we report in table .1. We also compute the rotation rates associated with these velocities at the surface of the star and deduce the equivalent orbital radius of a virtual planet (for a characteristic velocity V, the equivalent normalized orbital radius $r_{orb}/R_\star$ can be approximated by $(GM_\star/R_\star V^2)^{1/3}$, see Equation 6).

Table .1: Fiducial stellar wind parameters

Parameter	Value	Equivalent $r_{orb}/R_\star$
γ	1.05	...
$c_s/v_{\rm esc}$	0.2599	1.95
$v_A/v_{\rm esc}$	0.3183	1.7
$v_{\rm rot}/v_{\rm esc}$	0.00303	38

We intend to ultimately use our stellar wind model to study global close-in star-planet interactions in 3D. We choose a cartesian grid to avoid any future numerical issues that would be associated with very small grid cells at the stellar surface when using a curvilinear coordinate system with structured grids. The star is located at the center of our three-dimensional grid. In this work we consider two different static grid sizes to model stellar winds, the higher resolution being hereafter denoted HR. We also show one preliminary simulation using the AMR version of the pluto code. In the static version, the cube $[-1.5\,R_\star, 1.5\,R_\star]^3$ centered on the star is always uniformly discretized, and stretched grids are use in the three directions to grid the remaining of the domain up to $20\,R_\star$ from the star. The discretization is identical in the three dimensions.

In order to include a planet in such a stellar wind simulation, one can solve the MHD equation in a rotating frame rotating at the orbital rotation rate of the planet. The planet is then nicely at rest in the frame of the grid, and the stellar rotation rate needs just to be modified accordingly. Considering circular Keplerian orbits and neglecting the orbital motion of the star, the orbital rotation rate –that we use as the rotation rate of the rotating
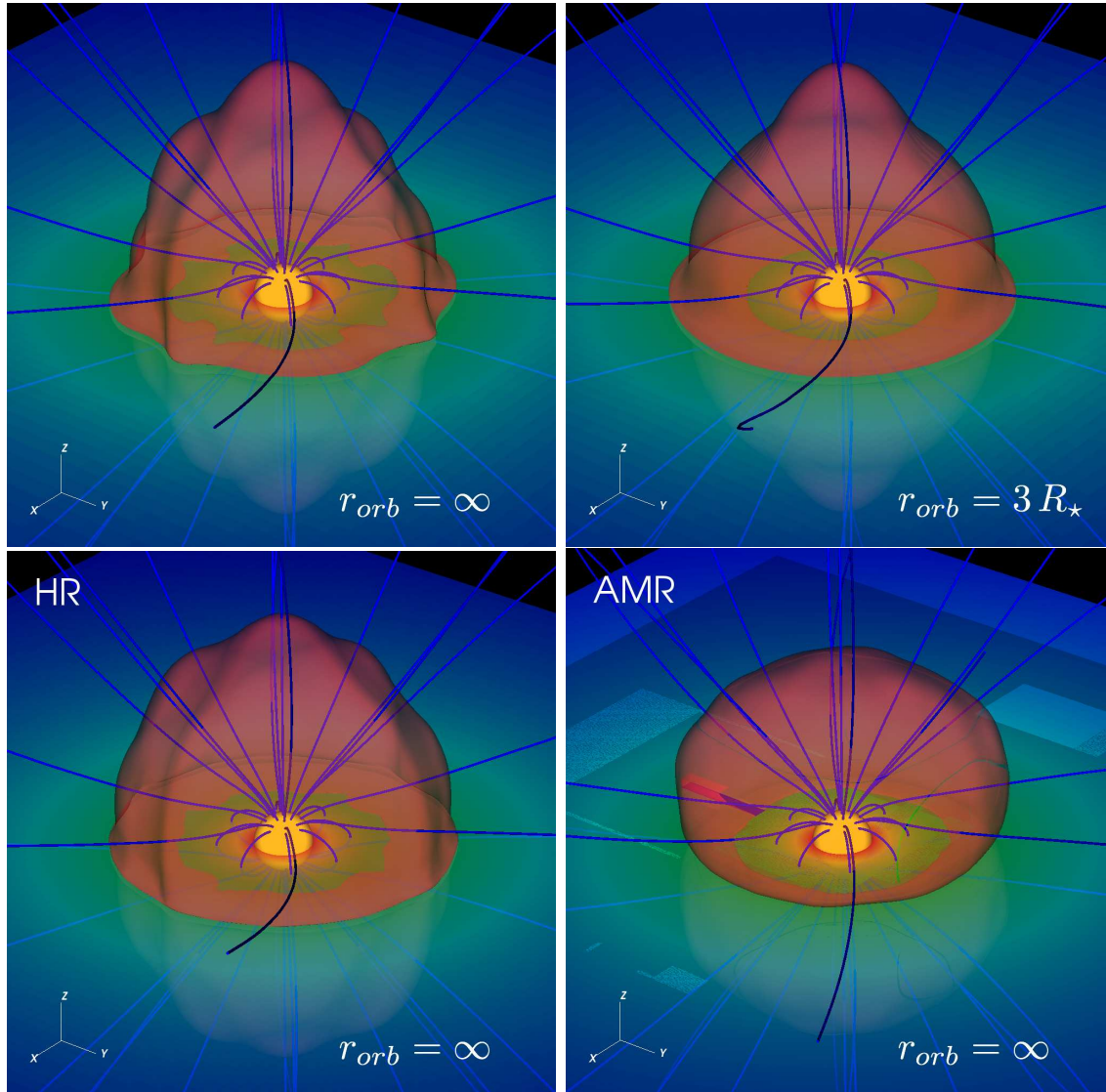
Figure .1: 3D renderings of the modelled stellar winds. The upper panels show cases 1 and 6, and the bottom panels cases 2 and 3 (see table .2). The stellar boundary is labelled by the orange sphere. The magnetic field lines are shown in blue and the Aflvén surface in transparent red. The density on the equatorial plane in shown in logarithmic scale, with the same color map on all the panels.

frame– of a planet located at r_{orb} is given by

$$\Omega_0 = \Omega_P = \sqrt{\frac{GM_\star}{r_{orb}^3}} \, . \tag{6}$$

In the following, even though we do not include any planet in the simulations yet, we label the various rotating frames we considered (listed in Table .2) by their equivalent orbital radius r_{orb} of the virtual planet. We express it in terms of breakup rotation rate $\Omega_b = (GM_\star/R_\star^3)^{1/2}$.

Table .2: Parameters of the stellar wind cases

Case	Resolution	$r_{orb}/R_\star$	Ω_0/Ω_b
1	225^3	∞	0
2 (HR)	449^3	∞	0
3 (AMR)	1920^3	∞	0
4	225^3	50	0.002
5	225^3	10	0.022
6	225^3	3	0.136
7 (HR)	449^3	3	0.136

3. Global properties of the modelled winds

We first illustrate our modelled stellar wind with three-dimensional visualizations of the cases 1, 2, 3, and 6 (see table .2) in Figure .1. In all the figures presented throughout this paper, the results have been transformed to the inertial frame to adequately compare the various cases.

Interestingly, the addition of a rotating frame seems at first glance to regularize the solution: the shape of the Alfvén surface (where the wind speed equals the local Alfvén speed) in case 1 (upper left panel) shows some non-axisymmetric features due to our cartesian grid whereas in case 6 (upper right panel, $r_{orb} = 3\,R_\star$) its looks perfectly axisymmetric. Nevertheless, despite this apparent regularization, the rotating frame induces significant (and non-axisymmetric) deviations in the stellar wind solution that could be problematic in the context of star-planet interactions models. We detail and quantify these deviations in the following sections. Higher resolution in the case with no rotating frame (lower panels, HR and AMR cases) clearly tend to reduce the non-axisymmetric aspect of the Alfvén surface.

3.1 Mass and angular momentum loss rates

We first assess the effect of the grid resolution and of the rotating frame on the integrated properties of the stellar wind. We define the mass and angular momentum loss rates due to the wind by

$$\dot{M}_\star = \oint \rho\mathbf{v}\cdot d\mathbf{A}\,, \tag{7}$$

$$\dot{J}_\star = \oint \varpi\left(v_\phi - B_\phi\frac{\mathbf{v}_p\cdot\mathbf{B}_p}{\rho|\mathbf{v}_p|^2}\right)\rho\mathbf{v}\cdot d\mathbf{A}\,, \tag{8}$$
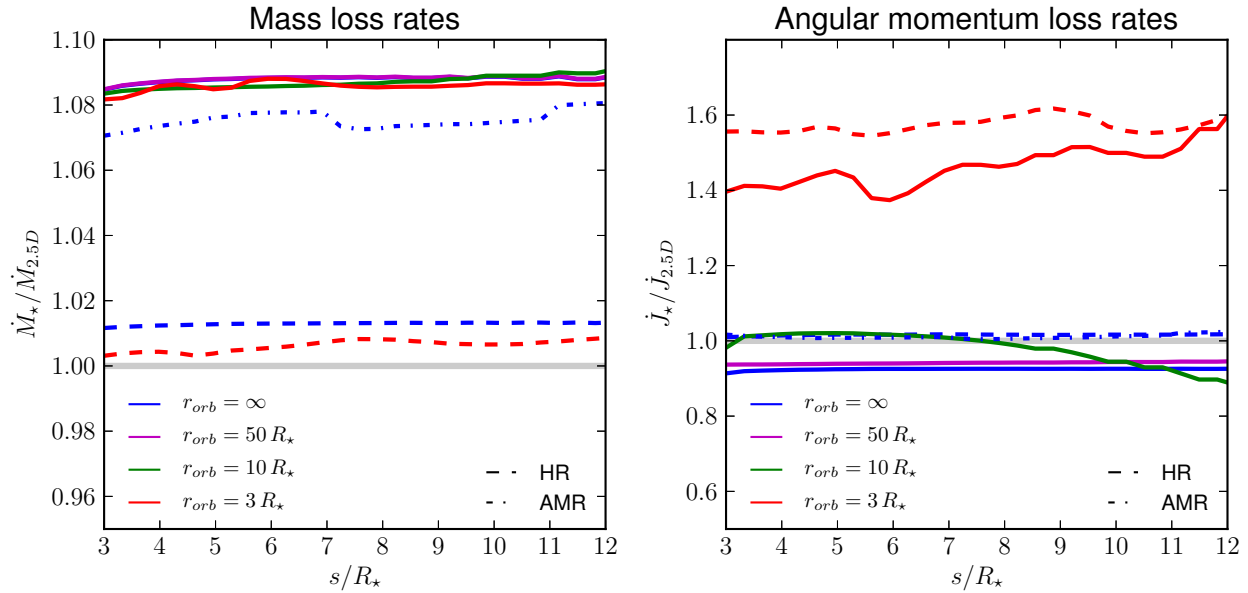
Figure .2: Mass and angular momentum loss rates as a function of the integration box [s] averaged over a few stellar rotations. The loss rates are normalized to the loss rates obtained from an equivalent 2.5D axisymmetric model (see Strugarek et al. 2014). The fiducial resolution cases are shown in solid line, the 'high' resolution (HR) cases in dashed lines and the AMR case in dash-dotted line. The various rotating frames are labeled with different colors.

where $\oint d\mathbf{A}$ represents the integral over a two-dimensional, closed surface. When a steady-state is reached, integrals (7-8) can be *in principle* equivalently evaluated on any surface enclosing the star. For instance we show in Figure .2 the loss rates computed with integrals over cubes of size $2\,s$ centered on the star ($\dot{M}_\star$ is shown in the left panel, and $\dot{J}_\star$ in the right panel). The loss rates are normalized to loss rates obtained from a 2.5D axisymmetric simulation (see Réville et al. 2014; Strugarek et al. 2014) with a resolution equivalent (in 2D) to the HR cases. We immediately see that the integrals are, in most of the cases, constant functions of s, indicating that a steady-state is reached and that mass and angular momentum are conserved in the flow.

The cases with no rotating frame are shown in blue (the solid line represents the fiducial resolution, the dashed line the 'high' resolution–HR and the dashed-dotted line the AMR case). The mass and angular momentum loss rates in the HR cases differ by less than 2% from the reference 2.5D simulation. The fiducial resolution cases differs from $\sim 10\%$ from the HR cases, which is a simple consequence of the very coarse resolution that was used in those cases. When a slowly rotating frame is added ($r_{orb} = 50\,R_\star$, magenta lines), only a marginal difference is observed in both loss rates.

We observe than the mass loss rates are mostly unaffected by the rotating frame: on the left panel each style of curve (solid and dashed) differ from less than 2% from one another. The angular momentum loss rate (right panel) is nonetheless severely altered when a rotating frame is added. The curves are even non-constant (cases with $r_{orb} \leq 10\,R_\star$ in green and red)

which is a due to the difficulty to get a steady-state for cartesian grids with high rotation rates Ω_0. Higher resolution (dashed red line) seems to help getting rid of those numerical issues, although in the case of $r_{orb} = 3\,R_\star$ the HR resolution should still be increased to adequately model the stellar wind and obtain a constant angular momentum loss rate consistent with the cases with no rotating frame.

3.2   Conservation properties

Using the cylindrical coordinates (ϖ, φ, z), and under the assumption of axisymmetry, five ideal-MHD quantities conserved along each magnetic field line can be defined by (see, *e.g.*, Lovelace et al. 1986; Ustyugova et al. 1999)

$$K(\psi) \equiv \rho \frac{\mathbf{v}_p \cdot \mathbf{B}_p}{|\mathbf{B}_p|^2} \,, \tag{9}$$

$$\Lambda(\psi) \equiv \varpi \left(v_\varphi - B_\varphi \frac{B_p}{\rho v_p} \right) = \varpi \left(v_\varphi - \frac{B_\varphi}{K} \right) \,, \tag{10}$$

$$\Omega_e(\psi) \equiv \frac{1}{\varpi} \left(v_\varphi - \frac{v_p}{B_p} B_\varphi \right) = \frac{1}{\varpi} \left(v_\varphi - \frac{K B_\varphi}{\rho} \right) \,, \tag{11}$$

$$S(\psi) \equiv P \rho^{-\gamma} \,, \tag{12}$$

$$E(\psi) \equiv \frac{1}{2} \left(\mathbf{v}_p^2 - v_\varphi^2 \right) + \frac{\gamma}{\gamma - 1} \rho^{\gamma - 1} S - \frac{GM_\star}{r} + v_\varphi B_\varphi \frac{K}{\rho} \,, \tag{13}$$

where ψ is a magnetic field line label and the subscript 'p' stands for the poloidal component of a vector field. Our initial and boundary conditions do not introduce *a priori* any non-axisymmetry (except maybe at the outer boundary). These five quantities should hence be conserved with a perfect model. The non-conservation can only arise from numerical errors, in our case principally due to the use of a cartesian grid which is not well adapted to the spherical geometry of the problem. In order to asses quantitatively the conservation properties of our 3D model, we compute on each three-dimensional field line the relative deviation from the field-line averaged conserved quantity Q, defined by

$$\bar{Q} \equiv \left| \frac{Q - \langle Q \rangle_{fl}}{\langle Q \rangle_{fl}} \right| \,, \tag{14}$$

where $\langle \rangle_{fl}$ stands for the average over one three-dimensional field line. We sample the surface of the star with 20 points in latitude and 3 points in longitude as seed points of magnetic field lines. We obtain in each cases approximately the same number of closed and open field lines.

We show in Figure .3 the normalized probability density function (PDF) of the relative deviation of conserved quantities for cases 1, 5, and 6. We restricted our analysis to the open field lines region, where the mass and angular momentum of the star are extracted by the wind. The PDFs of $\bar{K}$, $\bar{S}$, and $\bar{E}$ peak well below one and do not extend significantly above 10%. These three quantities can be considered, as a result, to be well conserved by our model. The PDFs of $\bar{\Lambda}$ and $\bar{\Omega}_e$ peak closer to 1 (above 10%) in the cases with a rotating frame (green and red). This is another way to see the numerical difficulty that is naturally imposed by our cartesian grid. The degree of non-conservation is sufficiently high so that the

wind models with $r_{orb} = 3\,R_\star$ and $r_{orb} = 10\,R_\star$ cannot be used reliably to, *e.g.*, derive general trends about stellar wind torques and mass loss rates. Note nevertheless that, at first glance, the solution $r_{orb} = 3\,R_{star}$ seemed perfectly well behaved (see Figure .1). The estimation of the angular momentum loss rate based on an integral over this regular Alfvén surface could not, in this case, provide an accurate calculation because of the lack of conservation of Λ we just highlighted.

We give more extensive statistical properties of the distributions of deviations in the open field lines region in table .3 for all the cases listed in table .2. It immediately appears that in all cases, the mean deviation (and its standard deviation) is the highest for $\bar{\Lambda}$ and $\bar{\Omega}_e$. The HR cases bring a significant improvement in the conservation of those two quantities, and in particular in their standard deviation. This shows that with a sufficiently high resolution, the angular momentum loss rate calculation could be robustly estimated from such three-dimensional models. The lack of conservation of Λ in stellar wind models is also generally accompanied by large longitudinal variations of the rotation rate of the wind. In the context of magnetic star-planet interactions, the rotation of the wind is naturally key to assess the eventual effect on the planetary magnetosphere and on the secular evolution of the system. As a consequence, only stellar wind models with acceptable conservation properties should be used to assess the effects of those interactions.

4.   Conclusions

We have presented a comparative study of simple, 3D models of the stellar wind of cool stars. We focused our study on the numerical problems that can arise from the use of *(i)* a cartesian grid and *(ii)* a (fast) rotating frame in the context of star-planet interactions.

Our results suggest that, without sufficient spatial resolution, a rotating frame with a rotation rate higher than the stellar rotation rate should be avoided. The numerical experiments presented here were conducted for a small stellar rotation rate. Because of this small rotation rate, small errors arising from the cartesian grid can lead to dramatic changes in the stellar wind solution. We expect the issues encountered in this work to be significantly lower in cases with higher stellar rotation rates, and adaptive mesh refinement seems to be an adequate, generic solution to overcome those numerical difficulties.

References

Cohen, O., & Drake, J. J. 2014, ApJ, 783, 55

Cohen, O., Drake, J. J., Kashyap, V. L., & Gombosi, T. I. 2009, ApJ, 699, 1501

Cuntz, M., Saar, S. H., & Musielak, Z. E. 2000, ApJ, 533, L151

Table .3: Statistics of the relative deviations of the conserved quantities (9-13) for open field lines.

		Mean	Standard Dev.	Skewness	Kurtosis
$r_{orb} = \infty$	$\bar{K}$	$7.0 \, 10^{-3}$	$2.5 \, 10^{-2}$	$2.3 \, 10^{1}$	$6.9 \, 10^{2}$
	$\bar{\Lambda}$	$4.9 \, 10^{-2}$	$5.0 \, 10^{-1}$	$1.2 \, 10^{2}$	$1.5 \, 10^{4}$
	$\bar{\Omega}_e$	$1.1 \, 10^{-2}$	$1.5 \, 10^{-2}$	6.0	$6.6 \, 10^{1}$
	$\bar{S}$	$9.8 \, 10^{-4}$	$1.3 \, 10^{-3}$	6.1	$7.0 \, 10^{1}$
	$\bar{E}$	$1.2 \, 10^{-3}$	$1.5 \, 10^{-3}$	6.7	$8.6 \, 10^{1}$
$r_{orb} = \infty$ (HR)	$\bar{K}$	$8.6 \, 10^{-3}$	$1.7 \, 10^{-2}$	$1.2 \, 10^{1}$	$2.3 \, 10^{2}$
	$\bar{\Lambda}$	$3.6 \, 10^{-2}$	$5.2 \, 10^{-2}$	$1.0 \, 10^{1}$	$1.9 \, 10^{2}$
	$\bar{\Omega}_e$	$1.0 \, 10^{-2}$	$1.5 \, 10^{-2}$	4.1	$2.7 \, 10^{1}$
	$\bar{S}$	$1.3 \, 10^{-3}$	$2.1 \, 10^{-3}$	8.2	$1.2 \, 10^{2}$
	$\bar{E}$	$1.5 \, 10^{-3}$	$2.2 \, 10^{-3}$	7.7	$1.1 \, 10^{2}$
$r_{orb} = 50 \, R_\star$	$\bar{K}$	$4.4 \, 10^{-3}$	$2.5 \, 10^{-2}$	$2.5 \, 10^{1}$	$7.9 \, 10^{2}$
	$\bar{\Lambda}$	$4.6 \, 10^{-2}$	$5.4 \, 10^{-1}$	$1.1 \, 10^{2}$	$1.4 \, 10^{4}$
	$\bar{\Omega}_e$	$3.7 \, 10^{-3}$	$6.6 \, 10^{-3}$	8.3	$1.4 \, 10^{2}$
	$\bar{S}$	$3.2 \, 10^{-4}$	$7.9 \, 10^{-4}$	$1.3 \, 10^{1}$	$2.4 \, 10^{2}$
	$\bar{E}$	$3.3 \, 10^{-4}$	$9.4 \, 10^{-4}$	$1.6 \, 10^{1}$	$3.4 \, 10^{2}$
$r_{orb} = 10 \, R_\star$	$\bar{K}$	$2.4 \, 10^{-2}$	$3.4 \, 10^{-2}$	9.8	$2.0 \, 10^{2}$
	$\bar{\Lambda}$	$3.1 \, 10^{-1}$	$6.9 \, 10^{-1}$	$6.1 \, 10^{1}$	$5.9 \, 10^{3}$
	$\bar{\Omega}_e$	$1.1 \, 10^{-1}$	$1.0 \, 10^{-1}$	1.7	3.5
	$\bar{S}$	$2.4 \, 10^{-3}$	$3.5 \, 10^{-3}$	3.4	$2.1 \, 10^{1}$
	$\bar{E}$	$2.3 \, 10^{-3}$	$3.9 \, 10^{-3}$	5.6	$5.4 \, 10^{1}$
$r_{orb} = 3 \, R_\star$	$\bar{K}$	$7.6 \, 10^{-3}$	$2.5 \, 10^{-2}$	$2.3 \, 10^{1}$	$6.8 \, 10^{2}$
	$\bar{\Lambda}$	$2.2 \, 10^{-1}$	5.7	$1.4 \, 10^{2}$	$2.1 \, 10^{4}$
	$\bar{\Omega}_e$	$7.2 \, 10^{-2}$	$6.5 \, 10^{-2}$	1.1	1.2
	$\bar{S}$	$4.4 \, 10^{-4}$	$1.2 \, 10^{-3}$	$1.8 \, 10^{1}$	$4.1 \, 10^{2}$
	$\bar{E}$	$6.4 \, 10^{-4}$	$1.5 \, 10^{-3}$	$1.9 \, 10^{1}$	$4.8 \, 10^{2}$
$r_{orb} = 3 \, R_\star$ (HR)	$\bar{K}$	$5.3 \, 10^{-3}$	$8.0 \, 10^{-3}$	$2.0 \, 10^{1}$	$6.2 \, 10^{2}$
	$\bar{\Lambda}$	$4.3 \, 10^{-2}$	$3.7 \, 10^{-2}$	1.7	5.2
	$\bar{\Omega}_e$	$2.8 \, 10^{-2}$	$2.7 \, 10^{-2}$	1.8	4.9
	$\bar{S}$	$3.1 \, 10^{-4}$	$5.5 \, 10^{-4}$	$1.3 \, 10^{1}$	$3.1 \, 10^{2}$
	$\bar{E}$	$3.7 \, 10^{-4}$	$6.9 \, 10^{-4}$	$1.9 \, 10^{1}$	$5.2 \, 10^{2}$

Laine, R. O., & Lin, D. N. C. 2011, ApJ, 745, 2

Lanza, A. F. 2009, A&A, 505, 339

—. 2014, arXiv, 6049

Lovelace, R. V. E., Mehanian, C., Mobarry, C. M., & Sulkanen, M. E. 1986, ApJS, 62, 1

Matt, S. P., MacGregor, K. B., Pinsonneault, M. H., & Greene, T. P. 2012, ApJ, 754, L26

Mestel, L. 1968, MNRAS, 138, 359

Mignone, A., Bodo, G., Massaglia, S., et al. 2007, ApJS, 170, 228

Mignone, A., Zanni, C., Tzeferacos, P., et al. 2012, The Astrophysical Journal Supplement, 198, 7

Oran, R., van der Holst, B., Landi, E., et al. 2013, ApJ, 778, 176

Parker, E. N. 1958, ApJ, 128, 664

Réville, V., Brun, A. S., Matt, S. P., & Strugarek, A. 2014, submitted to ApJ

Scharf, C. A. 2010, ApJ, 722, 1547

Sokolov, I. V., van der Holst, B., Oran, R., et al. 2013, ApJ, 764, 23

Strugarek, A., Brun, A. S., & Matt, S. 2012, in SF2A-2012: Proceedings of the Annual meeting of the French Society of Astronomy and Astrophysics. Eds.: S. Boissier, 419

Strugarek, A., Brun, A. S., Matt, S. P., & Réville, V. 2014, ApJ, 795, 86

Ustyugova, G. V., Koldoba, A. V., Romanova, M. M., Chechetkin, V. M., & Lovelace, R. V. E. 1999, ApJ, 516, 221

Vidotto, A. A., Jardine, M., Morin, J., et al. 2014, MNRAS, 438, 1162

Weber, E. J., & Davis, L. J. 1967, ApJS, 148, 217
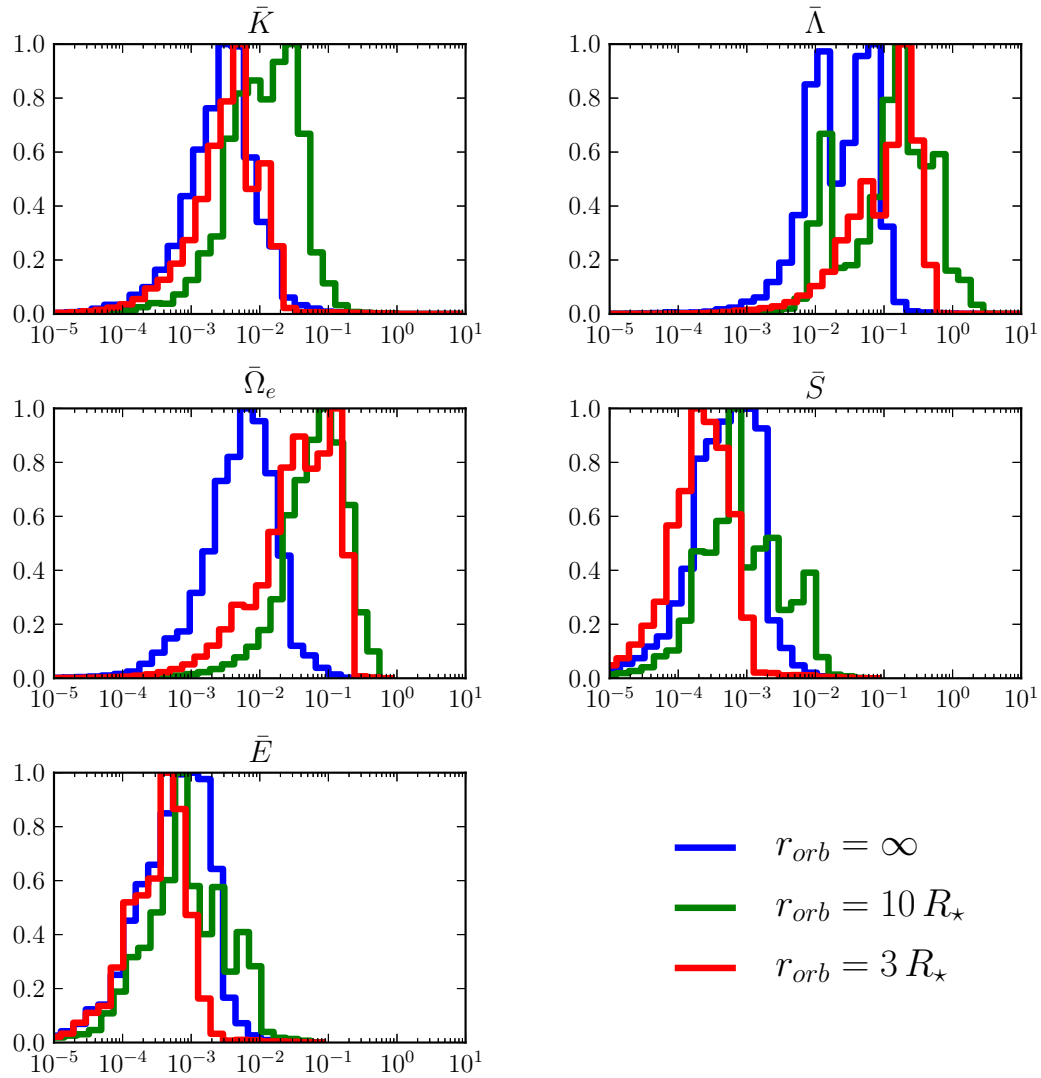
Zarka, P. 2007, Planet. Space Sci., 55, 598

Figure .3: Normalized probability distribution functions of the relative deviations of the conserved quantities (9-13) for open field lines. Case 1 is in blue ($r_{orb} = \infty$), case 5 in green ($r_{orb} = 10\,R_\star$) and case 6 in red ($r_{orb} = 3\,R_\star$). The three cases were run with the fiducial resolution (see table .2).

The Wednesday night public lecture was presented by Lucianne Walkowicz.

Cool Star Abundances